Reversibility and β-sheet formation are decoupled in tau condensate ageing

Charlotte M. Fischer,[1,†] Irina A. Edu,[1,†] Tomas Šneideris,[1,†] Ieva Baronaite,[1] Zenon Toprakcioglu,[1] Leif-Thore Deck,[1] Daoyuan Qian,[1] Rob Scrutton,[1] Lasse Dreyer,[1,2] Jitao Wen,[3] Daniel Otzen,[2] Si Wu,[3,4] Sarah Perrett,[1,3] Tuomas P. J. Knowles[1, *]

[1] Centre for Misfolding Diseases, Yusuf Hamied Department of Chemistry, University of Cambridge, Lensfield Road, Cambridge CB2 1EW, United Kingdom
[2] Interdisciplinary Nanoscience Center (iNano), Aarhus University, Denmark, Gustav Wieds Vej 14, 8000 Aarhus, Denmark
[3] Key Laboratory of Biomacromolecules (CAS), Institute of Biophysics, Chinese Academy of Sciences, 15 Datun Road, Chaoyang District, Beijing 100101, China
[4] University of the Chinese Academy of Sciences, 19A Yuquan Road, Shijingshan District, Beijing 100049, China

[†] Contributed equally
[*] Correspondence should be addressed to tpjk2@cam.ac.uk

Abstract

Neurofibrillary tangles (NFTs) formed from the protein tau disrupt neuronal function in Alzheimer's disease and are strongly associated with cognitive decline. Early events in tau aggregation are increasingly linked to the formation of biomolecular condensates, which lower the energetic barriers to pathological aggregation by acting as intermediates that transition into insoluble assemblies, a mechanism also implicated in other neurodegenerative diseases, such as amyotrophic lateral sclerosis (ALS) and frontotemporal dementia (FTD). Despite growing evidence for this pathway, the molecular basis by which reversible condensates evolve into irreversible, pathogenic aggregates has remained unclear. Here, we map the phase behaviour, structural transitions, and thermodynamic reversibility of tau during condensate ageing. Our results reveal that the two hallmark features of the pathological end state, β-sheet enrichment and irreversible aggregation, emerge at different rates and occupy distinct regions of the phase space, indicating that these properties are mechanistically uncoupled. Notably, we identify tau condensate phases that are β-sheet rich yet thermodynamically reversible, as well as irreversible intermediates that lack β-sheet structure. These findings expand the landscape of tau aggregate species beyond a simple linear progression toward fibrils and highlight a diverse array of intermediates with distinct structural and thermodynamic properties. This decoupling of structure and irreversibility has important implications for understanding tau aggregation mechanisms and may offer new targets for therapeutic intervention.

Significance

An aberrant phase transition of tau protein into insoluble protein aggregates is implicated in Alzheimer's disease. Growing evidence suggests that early tau aggregation can be mediated by biomolecular condensates. However, the process by which these reversible condensates become irreversible aggregates is unknown. Using combinatorial droplet-microfluidics, we measure time-resolved phase diagrams of tau and show that the two key properties of pathological aggregation, β-sheet structure and irreversibility, are mechanistically uncoupled. We reveal distinct intermediate phases, including some that are β-sheet rich yet reversible, and others that are irreversible but lack β-sheet structure. These findings expand our understanding of tau aggregation beyond a simple linear progression and highlight a more diverse array of intermediates, offering new insights and potential therapeutic targets.

Introduction

Tau is a microtubule-associated protein that plays a central role in Alzheimer's disease (1–6) and other neurodegenerative disorders known as tauopathies (7–9). In Alzheimer's disease, tau forms insoluble β-sheet-rich amyloid fibrils (10, 11) known as neurofibrillary tangles (12–17), a key pathological feature the abundance of which is correlated with the progression of the disease (1–6, 18). However, under physiological conditions, the intrinsically disordered protein tau, which is involved in microtubule polymerisation and stabilisation (19, 20), is highly soluble (21) and has been shown to undergo liquid-liquid phase separation (LLPS) (22–26) to form liquid-like condensates *in vivo* (27, 28), *in vitro* (1, 28–31) and on microtubule surfaces (27, 32, 33). Such liquid-phase tau condensates are dynamic, form in a fully reversible manner and are readily disassembled by living cells (27, 34); however, they are prone to undergo an ageing process, acquiring solid-like material properties (1, 28, 31, 34–39) and progressively losing their reversibility. Emerging evidence suggests that this liquid-to-solid transition, which has been observed in multiple disordered proteins, such as tau (1, 28, 31, 34–38), fused in sarcoma (FUS)(40, 41) and α-synuclein (42–48), is closely linked to neurodegeneration by promoting the formation of irreversible aggregates. Understanding the behaviour of tau across phases – from liquid-like to solid-like – is crucial for distinguishing its physiological from its pathological forms and vital for developing targeted therapies aimed at preventing or reversing tau aggregation in Alzheimer's and related tauopathies.

Despite its significance, a complete and systematic understanding of the physicochemical determinants of tau phases, the reversibility and β-sheet content of tau structures and the kinetics of solid-like structure formation from liquid-like condensates across the phase space is missing. Here, we show that the liquid-to-solid transition of tau condensates and the β-sheet formation from the dense phase are decoupled processes and follow different kinetics depending on the position in the phase diagram. Notably, this allows for the formation of β-sheet structures which are reversible within the first few hours.

To systematically map the phase boundaries of biopolymers based on their solubility and propensity to form β-sheet-rich structures over time, we have developed a high-throughput microfluidic platform. Our approach enables a high-resolution quantification of tau phase diagrams as a function of protein concentration, crowding and time, providing kinetic information about tau phase transitions as a function of the phase space. We pair this with dilute phase measurements in the two-dimensional phase space to shed light on the underlying mechanisms and tau interactions with other solutes leading to these phase transitions. Finally, it allows us to investigate tau ageing in the presence of agents that have been associated with promoting tau aggregation, such as heparin, revealing the active role of heparin in modulating tau interactions and accelerating tau ageing. Through this framework, we gain a mechanistic understanding of the thermodynamic and kinetic determinants of tau's phase transitions across the entire phase space, which reveals reversible and irreversible pathways shifting tau from functional soluble states to aggregated pathological states depending on the physicochemical conditions, suggesting a previously unrecognised window for therapeutic intervention by preventing or reversing aggregate formation.

Results and Discussion

Quantifying the liquid-to-solid transition of tau

A key challenge in studying the liquid-to-solid transition of biopolymers is the requirement to generate data over a large number of samples, each one of which has been prepared with a slightly different composition to allow exploring the full compositional phase space. To address this challenge, we have developed a high-resolution, high-throughput droplet microfluidic platform that enables systematic screening of full-length tau (2N4R tau, referred to as tau) phase behaviour across a multidimensional phase space. This approach allows us to precisely map the thermodynamic phase boundary of tau and then assess the reversibility of tau liquid or aged condensates using a dissolution assay (Fig. 1a) to quantify the kinetics of its liquid-to-solid transition. Using a previously developed platform PhaseScan (49), we generate droplets containing different concentrations of tau and polyethylene glycol (PEG) as a crowding agent in a microfluidic chip and image the droplets after incubation in the chip using a fluorescence microscope. This yields a phase diagram at an initial time point where every point in the phase diagram represents an imaged droplet, which is either homogeneous or contains tau condensates (Fig. 1b, S1a-d). After imaging, the droplets are collected and incubated for a desired time. To identify the fraction of droplets containing solid tau assemblies after incubation, picoinjection (50) is utilised to inject equal amounts of buffer into each droplet, lowering the tau concentration below the saturation concentration of phase separation and leading to the dissolution of liquid-like tau structures (Fig. 1c, Fig. S1e-g). Following picoinjection, the droplets are imaged to reveal the fraction of insoluble tau assemblies in the phase diagram.

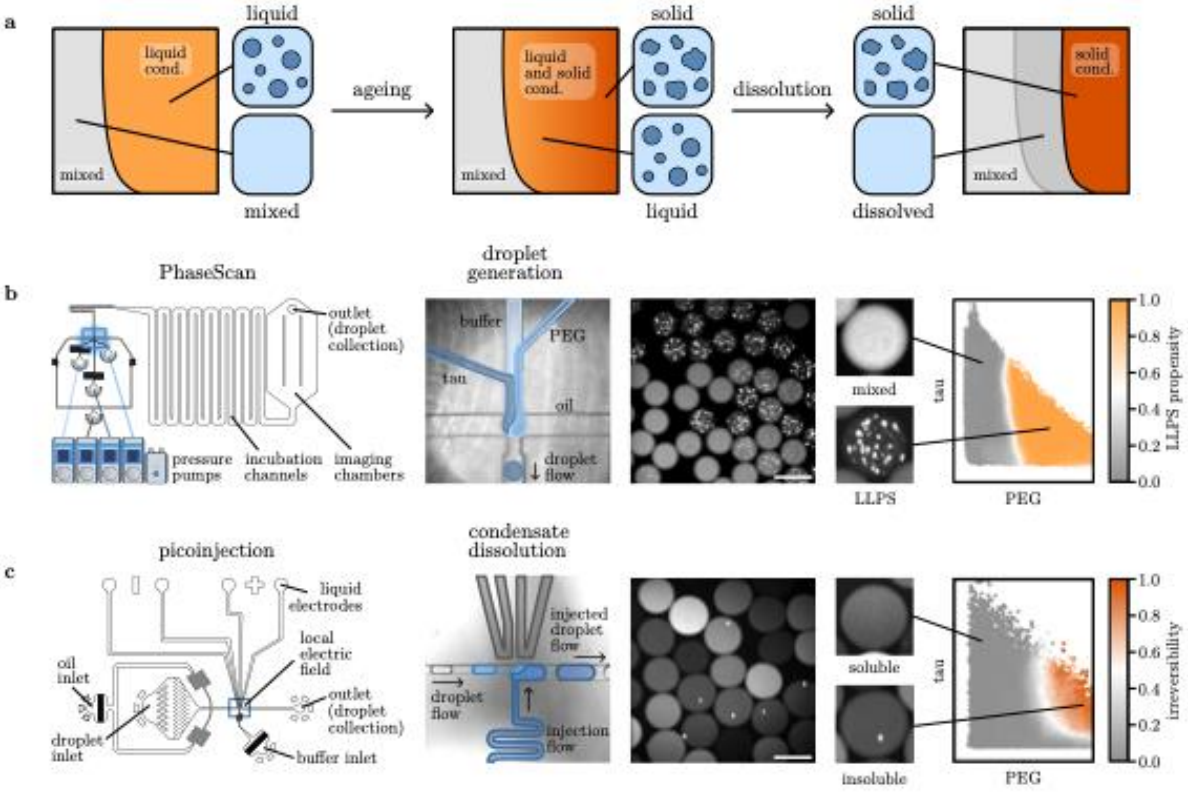

Figure 1. Microfluidic workflow of screening the liquid-to-solid transition of tau across the phase space and over time. **a.** Schematic phase diagrams of tau phase separation including initial LLPS and phase-space dependent condensate ageing. Aged condensates can be distinguished from liquid-like condensates through microfluidic dissolution. **b.** Microfluidic PhaseScan

chip used to measure tau phase diagrams at the initial time point by generating droplets containing varying concentrations of tau, PEG and buffer and imaging phase separated and mixed droplets using epifluorescence microscopy. Each droplet corresponds to one point in the phase diagram. **c.** Microfluidic picoinjection chip used to dilute each droplet sample resulting in the dissolution of liquid-like condensates. Aged solid-like condensates and dissolved droplets are imaged after picoinjection, yielding a phase diagram indicating condensate irreversibility. Scale bars are 200 µm.

Previously, it has been shown that crowding can accelerate ageing of liquid condensates for liquid-liquid phase separating protein systems (51). Here, we investigated the effect of the tau concentration and crowding on the ageing of tau condensates. First, we acquired a phase diagram of tau as a function of PEG concentration, mapping the binodal of the system separating the regions where tau is in solution or liquid-liquid phase separated at the initial time point (Fig. 2a, Fig. S2). We found that at concentrations of more than 8-10% PEG, crowding induces the formation of tau liquid condensates. With increasing tau concentration, less PEG is needed to induce liquid-liquid phase separation. The binodal of tau liquid-liquid phase separation is invariable over time as confirmed by imaging the tau droplets to acquire a new phase diagram after 24 h (Fig. S3). To map the region of solid-like aged condensates in the phase diagram as a function of time, we used the picoinjection dissolution assay (Fig. 1c, Fig. S1). The microfluidic droplets containing tau and PEG mixed at different ratios used to generate the phase diagram at the initial time point were incubated in a droplet collector for 42, 67, 97, 130, 148 and 220 min, respectively. Afterwards, the droplets were diluted using picoinjection, imaged and analysed to yield phase diagrams indicating regions in which droplets with a corresponding concentration of tau and PEG contain either soluble or insoluble protein assemblies (Fig. 2b). Initially, all condensates are soluble up to 42 min of incubation. With time, the fraction of droplets containing insoluble tau assemblies increases. Droplets containing high concentrations of PEG age faster, at above 13% PEG condensates age after only 67 min, while condensates close to the liquid-liquid phase separation saturation concentration around 10% PEG age only after 220 min. The apparent increase in reversibility at 148 min at concentrations below 3 µM tau is attributed to experimental uncertainty of microfluidic dilution experiments at low levels of protein due to the low fluorescence intensity of the protein, resulting in a lower signal-to-noise ratio. Our findings indicate that crowding accelerates the transition of tau condensates from a soluble liquid-like to an insoluble solid-like state. These results are in agreement with dissolution experiments performed in bulk as well as fluorescence recovery after photobleaching (FRAP) recovery rates of tau-PEG condensates formed in bulk (Fig. S4, S5). Further, using confocal fluorescence microscopy imaging, we confirmed that aged tau condensates do not merge upon contact with each other, indicating solid-like material properties (Fig. S6).

To further elucidate how changes in tau molecular interactions could lead to the observed phase behaviour, we quantified the dilute phase concentration of tau as a function of the total tau concentration in each droplet for different concentrations of PEG (Fig. 2c, Fig. S7). We found that at increasing concentrations of PEG, the response gradient R, indicating the partitioning of tau between the dilute and dense phase, decreases, as more tau partitions from the dilute into the dense phase. The tau dilute phase measurements allowed us to determine the dominance (52, 53) of tau (Fig. 2d), the ratio of the free energy contribution of tau-tau interactions to the total free energy of tau phase separation, which can be expressed as a sum of contributions of each individual solute in the system. The dominance D and the response gradient are linked by the relationship $D = 1 - R$. We determined the dominance of tau in a range of 5-12% PEG and found that with increased crowding above 8% PEG, the dominance increases, along with the recruitment of tau from the dilute into the dense phase.

The high dominance of tau above 8% PEG indicates that tau-tau interactions are the main driving force for tau phase separation in the tau-PEG system.

Further, by mapping the dilute phase concentration of tau across the phase diagram and sectioning it for thresholds with $a < c_{dil} < b$, we obtained lines with a constant dilute phase concentration. Under the conditions we used, these lines of constant dilute phase concentration in the two-dimensional phase diagram recapitulate well the thermodynamic tie lines (53–58). The conditions along a tie-line have identical dilute and dense phase concentrations and allow us to assess the ratio of the two solutes, tau and PEG, in the dilute and dense phase. Fitting the dilute phase bands of tau across the tau-PEG phase diagram yields a positive and high tie-line gradient *K* (Fig. 2e). This is an indication of strong partitioning of tau into the condensates and a small enrichment in PEG and suggests a major role of tau-tau and a minor role tau-PEG interactions in phase separation, in agreement with the energy dominance analysis above. Further, the tie-line gradient measurement suggests that the dense phase composition of the two-component tau-PEG system changes across the phase space, such that the material properties of condensates could differ. To probe the effect of the PEG concentration on the mobility of tau molecules within the condensates (Fig. S8a,b), we performed FRAP experiments. Tau condensates formed at 12% PEG exhibited a faster recovery after photobleaching compared to condensates formed at 24% PEG, indicating that at high PEG concentrations the dense phase viscosity is increased and mass transport inside tau condensates is slowed down, leading to more solid-like material properties of the condensates. We hypothesise that these differences in the dense phase composition and dense phase mobility across the phase space could be responsible for the different ageing behaviour of tau condensates.

Next, the nature of the tau-tau interactions that underlie tau LLPS were explored. First, we tested the effect of salt, sodium chloride, on tau phase separation. It was observed that tau phase separates under low to moderate salt concentrations, while high salt concentrations dissolve tau condensates (Fig. S9a). This indicates that tau phase separation is most likely driven by electrostatic tau-tau interactions, which is in agreement with previous studies on tau phase separation (59, 60). The dilute phase bands in the tau-salt phase diagram exhibit a negative slope in the phase separated region, indicating a higher concentration of tau and a lower concentration of salt in the dense phase compared to the dilute phase, suggesting negative interactions between the two solutes (Fig. 9b). Further dominance analysis of tau as a function of salt concentration (Fig. S9c) indicates a decrease in tau dominance, i.e. tau-tau interactions, as the salt concentration increases, leading to dissolution of condensates by disruption of tau electrostatic interactions. The idea that tau electrostatic interactions drive its phase separation was further confirmed by the observation that at sufficiently low salt concentrations, tau phase separates at low PEG concentrations of 2%, and even in the absence of PEG, while increased salt concentrations dissolve the condensates (Fig. S10a,b). Additionally, we probed whether hydrophobic interactions could play a role in tau condensation. 1,6-hexanediol was used to test the stability of tau condensates against hydrophobic disruption (Fig. S11). Addition of 1,6-hexanediol did not dissolve tau condensates, which suggests that hydrophobic effects play a negligible role in tau phase separation.

Further, we used confocal microscopy detection to investigate the changes in the tau dilute phase with time (Fig. 2f). To measure the dilute phase, we flowed samples through a microfluidic channel and read out the fluorescence intensity of the protein at one location in

the channel under sample flow (Fig. S12). The dilute phase concentrations were extracted from the baseline signal of the condensate solution, while the dense phase was detected as short bursts of high fluorescence intensity signal due to the high tau concentration inside of condensates (61) We find that the dilute phase concentration of tau decreases as condensates age, indicating that tau-tau interactions increase leading to higher recruitment of tau from the dilute phase into the dense phase (Fig. 2f, Fig. S13). Between 0 h and 24 h, the concentration of the dilute phase decreases monotonically until a plateau is reached. At this point, the dilute phase has equilibrated with the new solid phase. Knowledge of the dilute phase concentration of tau at this time (termed c_{solid}) allows computing the free energy change (i.e. the driving force) of solidification, as to $\Delta G = -RT \ln \frac{c_{liquid}}{c_{solid}}$, where R denotes the gas constant and c_{liquid} the dilute phase concentration that is in equilibrium with the condensates before solidification, which is set to the first value measured. In principle, additional species such as PEG and the buffer ions may contribute to the free energy change. Given that the dominance analysis indicated that tau dominates the energetic landscape of this phase transition, their exclusion from the calculation appears justified. Applying the equation results in energies of −0.26 ± 0.05 and −0.27 ± 0.06 kcal/mol for 7.5 and 10 µM tau with 10% PEG, and −0.69 ± 0.15 and −0.73 ± 0.20 kcal/mol for 7.5 and 10 µM tau with 15% PEG. All four values are rather small in absolute terms, comparable with the energetic differences between polymorphic forms in the crystallization of small molecules (62). The kinetics of any phase transition - be it driven by nucleation, growth, or other microscopic phenomena - all scale with ΔG, such that values close to zero give an indication that a transition may be slow, in line with the observations made here. The finding of a larger driving force for 15% PEG than for 10% PEG aligns with the observation that the transition occurs faster at higher PEG concentrations. We conclude that an increase in tau interactions driven by crowding or emerging with time leading to a stronger protein network is responsible for the transition of liquid tau condensates into insoluble tau assemblies (Fig. 2g).

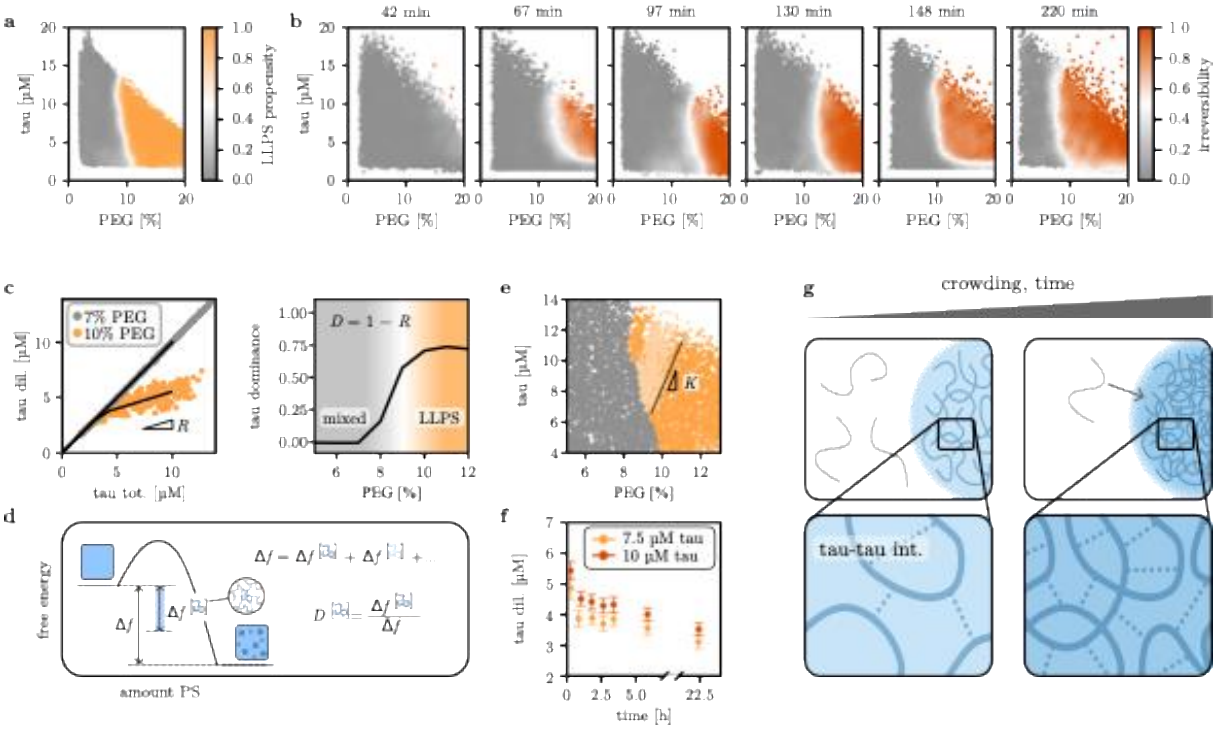

Figure 2. Quantifying the liquid-to-solid transition of tau as a function of the two-dimensional phase space using ultra high-throughput droplet microfluidics. **a.** Phase diagram of tau liquid-liquid phase separation at the initial time point. **b.** Representative phase diagrams out of 13 measurements showing the irreversible solid fraction of the tau phase space after

42, 67, 97, 130, 148 and 220 min of incubation, respectively, as determined by a microfluidic dissolution assay. The phase diagrams were cropped based on the population of droplets diluted sufficiently for the protein and PEG inside the droplet to have a concentration significantly below the saturation concentration. **c.** Left: Tau dilute phase as a function of the total tau concentration at 7% and 10% PEG, indicating a decrease in the dilute phase concentration at higher PEG concentrations. The dominance *D* was calculated using *D = 1-R* after fitting the response function *R* for PEG concentrations between 5 and 12%. Right: Dominance of tau as a function of PEG concentration at the initial time point, indicating stronger tau-tau interactions at increased crowding. **d.** Dominance representing the free energy contribution of one solute divided by the total free energy of phase separation, which can be written as a sum of the free energy contributions of each solute. **e.** Dilute phase bands of tau as a function of PEG concentration and linear fit of the dilute phase band gradient *K*, the positive slope indicating attractive tau-PEG interactions. **f.** Decrease of the dilute phase concentration of tau within the phase separated regime with time. The dilute phases were measured at 10% PEG and 7.5 and 10 μM tau, respectively. **g.** Schematic representing the increase in tau interactions with time and as a function of increased crowding, leading to stronger network interactions and lower solubility of the tau assemblies.

Measuring tau ageing kinetics across the phase space

Based on our findings, the liquid-to-solid transition of tau protein occurs at different times depending on the position in the two-dimensional phase space. We analysed the kinetics of tau liquid-to-solid transition as a function of tau and PEG concentration using a grid approach to map the half times of the liquid-to-solid transition as a function of the two-dimensional phase space (Fig. 3a). For each position in the grid at each time, the fraction of droplets containing solid-like tau assemblies (irreversible fraction) is calculated with respect to the total number of droplets (which may contain soluble or insoluble tau assemblies). This yields an estimated score of likelihood of tau condensate irreversibility for each grid point. From this data, an irreversibility trace over time is plotted for each grid position (Fig. 3b,c, two examples are indicated with black arrows), the inflection point of the fit indicating the estimated half-time of the liquid-to-solid transition. Using this data, we simultaneously calculated the half-time of the liquid-to-solid transition as a function of the entire two-dimensional phase space by fitting the irreversibility traces of each grid position. Our data indicate that the half-time of the liquid-to-solid transition has a strong phase space-dependency, being highly sensitive to the concentration of PEG, and less sensitive to the concentration of tau. The fastest liquid-to-solid transitions occur at high tau concentrations in a highly crowding PEG environment.

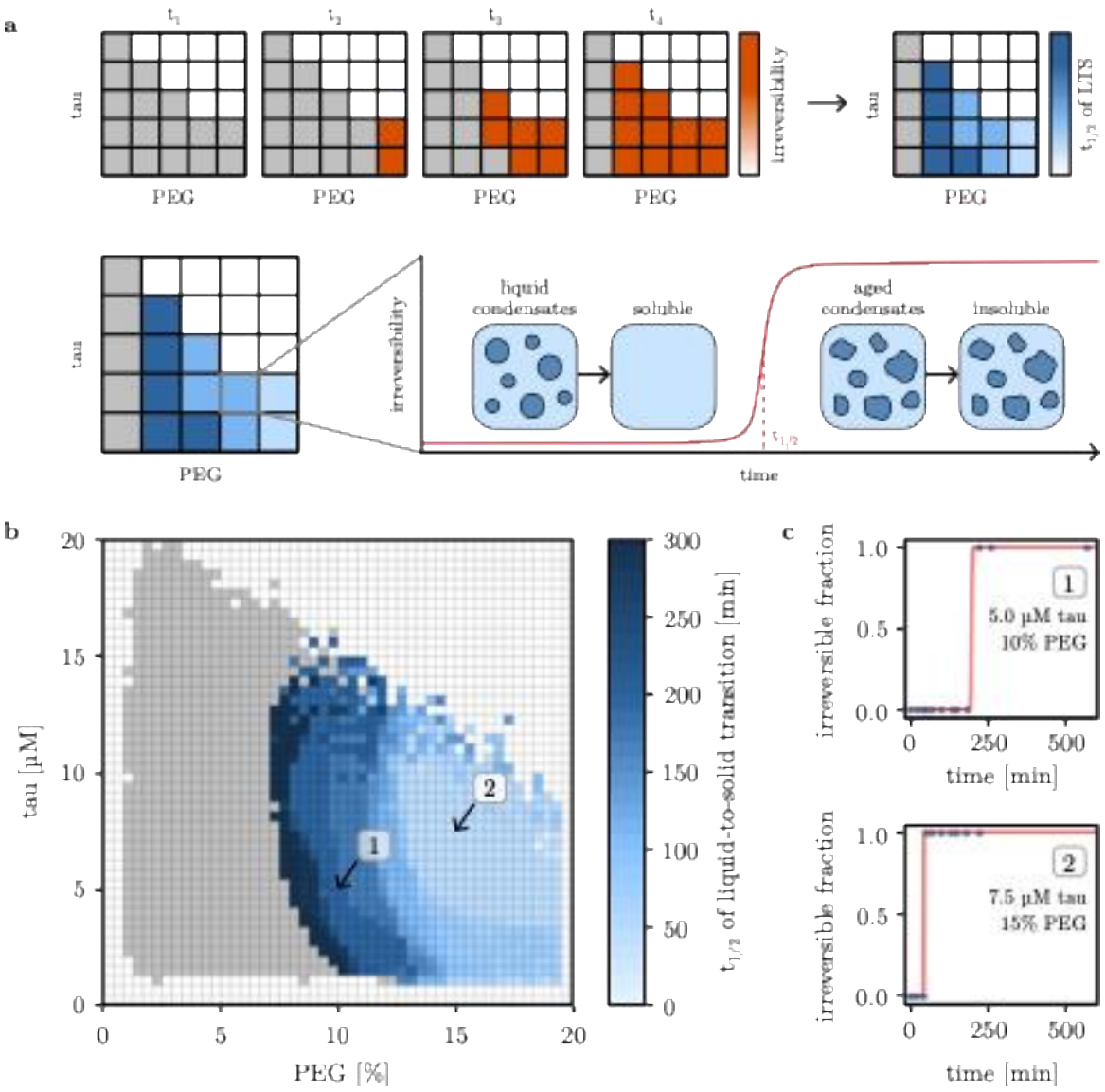

Figure 3. Tau liquid-to-solid transition kinetics in the two-dimensional phase space. **a**. A grid-based approach is used to determine tau ageing kinetics. A probability of irreversibility (orange) is assigned to each grid point for each time point, respectively. For each grid point, the irreversibility trace as a function of time is fitted using a sigmoidal fit, from which the half-time of the liquid-to-solid transition is calculated and shown as a heat map (blue). **b.** Heat map indicating the half-times of the liquid-to-solid transition as a function of the concentration of tau and PEG. **c.** Irreversible fractions and sigmoidal fits of the liquid-to-solid transition of tau as a function of time for two individual grid points (black arrows) at 5 μM tau, 10% PEG and 7.5 μM tau, 15% PEG respectively.

Investigating the reversible and irreversible β-sheet transition of tau

The formation of tau β-sheets is directly linked to neurodegeneration by the observation of neurofibrillary tangles (63, 64) in Alzheimer's patients, which exhibit a fibrillar amyloid structure. Hence, classic tau aggregation kinetic studies are mainly focused on the formation of β-sheet rich structures from monomeric tau in solution and the most common technique to study this is by using plate reader assays and measuring the increase in fluorescence of amyloid-binding dyes, such as Thioflavin T (65) or Amytracker (66), which change their quantum yield as a response to a restriction in the dye's rotational freedom upon binding to β-sheets. However, classic tau aggregation assays fail to capture information on the whole phase space, are not able to detect protein assemblies that are not active in ThT, or the early β-sheet structures where the increase in the quantum yield of the dye is minimal and cannot

differentiate between β-sheet originating from the homogeneous, dilute or dense phases. Moreover, they do not inform about the reversibility of any of these phase transitions. Hence, we developed a microfluidic-based assay using Amytracker680 dye, which allows us to track the formation of β-sheet-rich structures in the tau-PEG phase space over time and from which phase they originate as well as quantify the kinetics of both the early reversible β-sheet and the irreversible β-sheet formation (Fig. 4a).

To monitor the formation of β-sheet structures in the tau-PEG phase space, we generated droplets with unlabelled tau and PEG that contain a constant concentration of Amytracker680 dye. We incubated the droplets for 33, 76, 121, 181, 241, 361 and 1051 min, respectively, and imaged them after incubation to generate phase diagrams at different time points - here we detected tau β-sheet structures as Amytracker680 fluorescent features as they emerge with time (Fig. 4b). A minor enhancement of phase separation at the initial time point due to the addition of Amytacker680 dye was observed, as indicated by a shift of the LLPS boundary towards lower PEG concentrations independently of the protein concentration (Fig. S14). While condensates at the initial time point have a low intensity in Amytracker680 fluorescence and are not detected as features (Fig. S15), we detected droplets containing the first Amytracker680-positive, β-sheet rich structures emerged from tau condensates in the LLPS regime above 8% PEG at high tau concentrations as early as 33 min. The effect of Amytracker680 dye concentration on the emergence of fluorescent features over time was found to be of little relevance within the probed dye concentration range spanning an order of magnitude (Fig. S16). Over a total of 1051 min, the region of the phase diagram containing β-sheet rich structures expands to areas with a lower total tau concentration around 5 μM. During this time, no β-sheet formation occurs from the mixed phase (67), indicating that the transition of tau towards forming β-sheets is highly accelerated by tau liquid-liquid phase separation (29). Interestingly, the formation of β-sheet structures is facilitated by high tau concentrations as well as moderate ranges of crowding agent. By contrast, this process is slowed down on the timescales of our experiment in tau condensates formed under high-PEG conditions. We further analysed the kinetics of tau β-sheet formation mapping the phase-space dependency of the half-times of the transition (Fig. 4c), following the same approach as in the section above. We find that tau β-sheet formation occurs on a timescale between 0 and 300 min from liquid condensates. These findings suggest that compared to tau aggregation from homogeneous solution, liquid-liquid phase separation accelerates tau aggregation (Fig. 4d), which is in good agreement with previous work showing that LLPS of phosphorylated tau precedes aggregation (31, 68).

Furthermore, to confirm structural changes and β-sheet formation, Fourier transform infrared spectroscopy (FTIR) measurements were taken (Fig. S17a,b). Spectra of fresh tau samples containing 10 μM tau and 12% and 20% PEG, respectively, were measured and characteristic amide I and II peaks of random coil conformation were observed. For samples with 12% PEG, a shift to lower wavenumbers was observed after 6 h, respectively, suggesting the presence of β-sheet structures. For samples containing 20% PEG, a random coil conformation was retained over time, in agreement with the β-sheet propensity phase diagrams (Fig. 4b). As FTIR is a bulk method and lacks spatial resolution, FTIR spectra are a superposition of signals from both the protein dilute and dense phase. Consequentially, longer timescales are required to measure tau β-sheet formation. Therefore, FTIR was primarily used to confirm the presence of sheets, while kinetic information was extracted from the microfluidic assay.

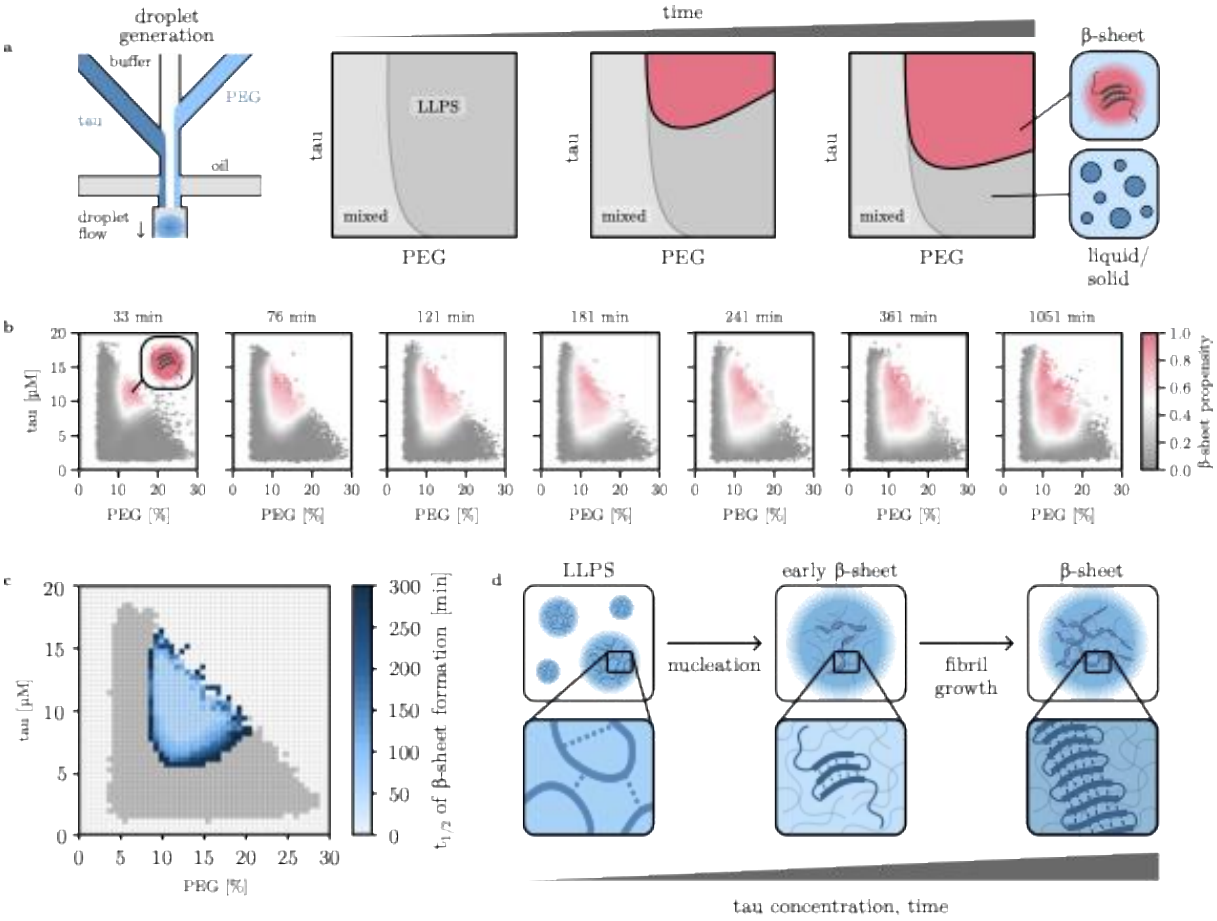

Figure 4. Early formation of tau β-sheet rich structures from the high-tau phase separated regime. **a.** Workflow of the microfluidic assay used to detect β-sheet-rich structures. Droplets containing fluorescently barcoded tau and PEG in different ratios as well as a constant concentration of Amytracker680 dye are generated, collected and imaged in a sealed glass imaging chamber over time **b.** Representative phase diagrams showing the β-sheet propensity of tau assemblies as a function of the tau-PEG phase space, indicating the formation of β-sheet rich structures after 33, 76, 121, 181, 241, 361 and 1051 min, respectively. **c.** Heat map indicating the half-times of tau β-sheet formation in the two-dimensional phase space. **d.** Schematic indicating how liquid-liquid phase separation can enhance tau β-sheet formation by increasing the interactions of tau in the dense phase.

Modulating tau liquid-liquid phase separation and liquid-to-solid transition using heparin

Heparin is a negatively charged biopolymer commonly used in tau kinetic measurements to induce tau aggregation (69–73). However, very little is known about the mechanism of how heparin modulates tau aggregation kinetics or the effect of heparin on other states of tau. Here, we assess the effect of heparin on tau LLPS and liquid-to-solid transition. Using our microfluidic platform, we show that at the initial time point, heparin shifts the LLPS boundary of the tau-PEG system towards a lower saturation concentration of only 5-6% PEG needed to induce tau phase separation (Fig. 5a, Fig. S18). Next, we investigated the effect of heparin on the liquid-to-solid transition of tau. As introduced above, we used picoinjection to quantify the solid-like fraction of the droplets after 40, 57, 158, 325 and 466 min and found that heparin accelerates the liquid-to-solid transition. A fraction containing solid condensates above 10% PEG already formed after 57 min and up to almost 7% PEG already at 158 min (Fig. 5b), whereas in the absence of heparin the solid fraction reached 10% PEG only around 148 min (Fig. 2b). The apparent increase in reversibility at 325 min at low tau concentrations is attributed to experimental uncertainty due to a low signal-to-noise ratio in that part of the phase space. Using confocal fluorescence microscopy imaging, we confirmed that aged tau-

PEG condensates formed with heparin do not merge, indicating solid-like material properties (Fig. S19). We mapped the kinetics of the liquid-to-solid transition in the two-dimensional phase space and calculated the half-times of the transition (Fig. 5c). Intriguingly, the half-times of tau vs PEG in the presence of heparin are significantly lower than the half-times without heparin. To understand the molecular mechanism of this modulation of the liquid-to-solid transition of tau, we mapped the propensity of tau to form liquid condensates as a function of the heparin concentration in the presence of 6.4% PEG, which is not sufficient to induce tau phase separation in the absence of heparin. We find that above concentrations of 2.5 µM tau, heparin can induce phase separation of tau for tau:heparin ratios >1:12.5 and that increasing heparin concentrations increase tau-tau interactions, leading to a higher phase separation propensity (Fig. 5d, Fig. S20). Only at tau:heparin ratios of <1:12.5, heparin has a dissolving effect on tau condensates due to the high negative charge of heparin leading to electrostatic repulsion destabilising the condensates. We analysed the dilute phase bands of tau vs heparin (Fig. 5e, Fig. S21) to assess the ratio of tau and heparin in the dilute and dense phases – the positive gradient indicates a higher concentration of tau and heparin in the dense phase than in the dilute phase, and hence an attractive interaction between tau and heparin over a wide range of heparin concentrations. This is most likely based on electrostatic interactions between the negatively charged heparin and tau. We further determined the dominance of tau as a function of the heparin concentration to reveal an increase in tau-tau interactions with increasing heparin concentration (Fig. 5f, Fig. S22). The data suggests that heparin accelerates the liquid-to-solid transition of tau by co-partitioning with tau in the condensates and strengthening the tau-tau interactions.

For a complete picture of the action of heparin, we investigated the β-sheet formation propensity across the tau-PEG phase space in the presence of heparin over time. Phase diagrams generated by imaging droplets containing unlabelled tau and PEG and a constant concentration of heparin were acquired at 0, 59, 119, 189 and 469 min, respectively (Fig. 5g). Interestingly, already immediately after droplet generation, β-sheet structures are detected in the phase separated region at high tau concentrations and moderate PEG concentrations for tau-PEG ratios of above 1:2 (Fig. 5g, Fig. S23). At low tau and high PEG concentrations, we again observe a slower formation of β-sheets, likely due to the higher viscosity in the dense phase due to higher amounts of PEG. In comparison to the tau β-sheet formation in the absence of heparin, the presence of heparin lowers the saturation concentration of phase separation and thereby allows for the formation of β-sheets in a wider range of the phase space. At the same time, heparin accelerates the β-sheet formation, likely by increasing tau-tau interactions, so that already after 469 min β-sheet formation can be observed at tau concentrations up to 20 µM at above 5% PEG. Analysis of the half-times of the β-sheet transition in the presence of heparin across the tau-PEG phase space (Fig. 5h) confirmed this observation, indicating that heparin accelerates not only the liquid-to-solid transition of tau, but also the β-sheet formation.

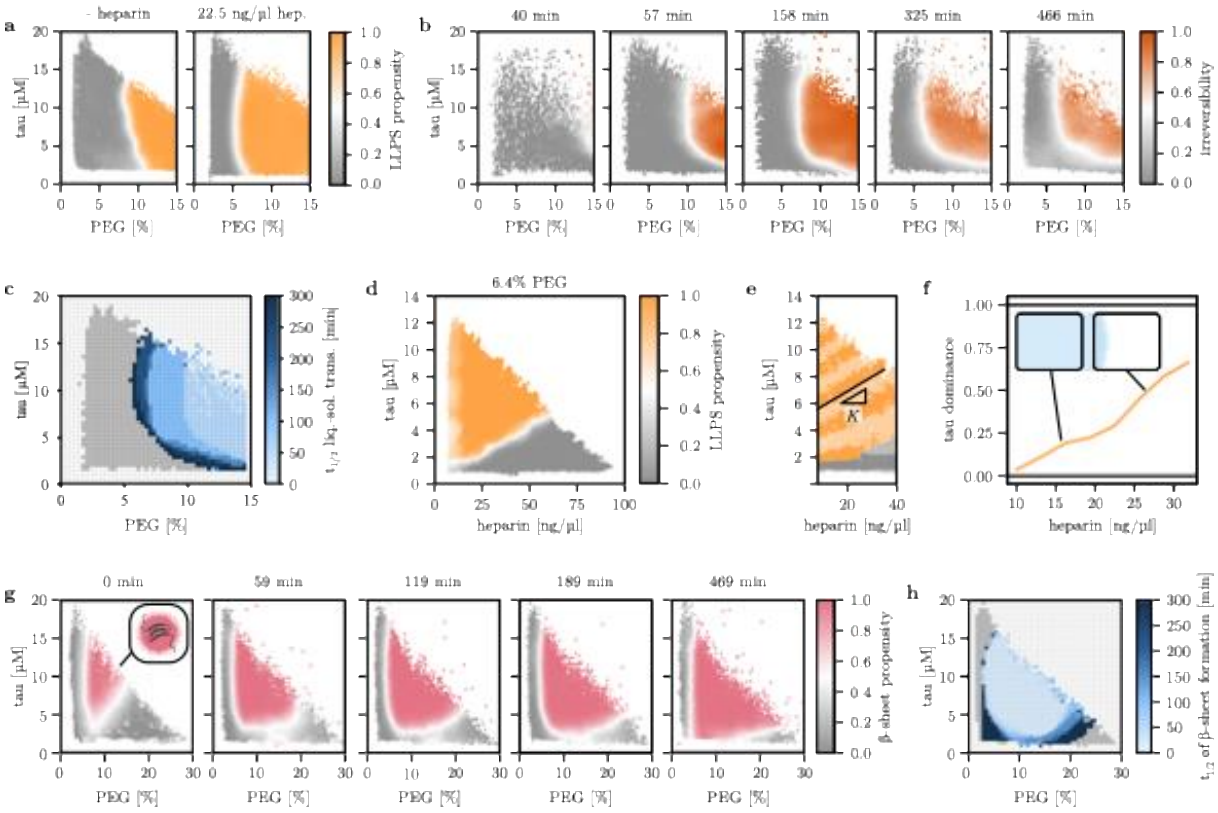

Figure 5. Enhancing effect of heparin on the liquid-liquid phase separation and liquid-to-solid transition of the tau-PEG system. **a.** Comparison of the phase boundaries for liquid-liquid phase separation in the tau-PEG phase space +/- 22.5 ng/µl heparin, indicating a shift towards a c_{sat} at lower PEG concentrations with heparin. **b.** Representative phase diagrams showing the solid fraction of the tau-PEG phase space in the presence of const. 22.5ng/µl heparin at 40, 57, 158, 325 and 466 min, respectively. The phase diagrams were cropped based on the population of droplets diluted sufficiently for the protein and PEG inside the droplet to have a concentration significantly below the saturation concentration. **c.** Heat map indicating shorter/faster liquid-to-solid transition half-times for tau in the presence of 22.5 ng/µl heparin. **d.** Phase diagram of tau as a function of heparin at 6.4% PEG, indicating that heparin can induce tau phase separation at low to medium heparin concentrations and inhibit phase separation at high heparin concentrations. **e.** Positive dilute phase band gradient of the tau-heparin system, indicating positive interactions of tau with heparin for heparin concentrations up to 40 ng/µl heparin. **f.** Tau dominance as a function of heparin concentration at const. 6.4% PEG, indicating an increase in tau-tau interactions leading to higher recruitment of tau into the dense phase as a function of heparin. **g.** Representative phase diagrams showing the β-sheet propensity of tau assemblies as a function of the tau-PEG phase space in the presence of 22.5 ng/µl heparin, indicating the formation of β-sheet rich structures after 0, 59, 119, 189 and 469 min, respectively. **h.** Heat map indicating the half-times of the β-sheet formation as a function of the concentration of tau and PEG in the presence of 22.5 ng/µl heparin.

Integrating tau insolubility and β-sheet propensity in the two-dimensional phase space

By integrating the data from the solubility assay with the β-sheet phase diagrams, we can generate overlay phase diagrams which give comprehensive information regarding the state, the reversibility and the β-sheet content of the tau assemblies formed at any given position in the phase diagram (Fig. 6a). In particular, we analysed and compared here the reversibility and β-sheet content of tau as a function of PEG concentration at 45, 133 and 223 min, respectively (Fig. 6b). We find that at low tau concentrations, liquid-liquid phase separation occurs at moderate to high crowding levels, and these condensates undergo a liquid-to-solid transition into amorphous protein assemblies which is dependent on time and the concentration of PEG. At higher concentrations of tau and moderate crowding conditions, we observe the formation of β-sheets from the liquid-liquid phase separated state. Notably, the formed β-sheet structures are soluble for the first hours after their formation, with the concentration of PEG influencing the rate of their liquid-to-solid transition leading to irreversible β-sheet structures. At high PEG concentrations, the formation of β-sheet-rich

structures was not observed on the timescale of our experiment. Interestingly, the formation of amorphous tau assemblies and β-sheet-rich structures from condensates happens at different timescales depending on the position in the phase diagram and can be reversible or irreversible, suggesting that those processes are mechanistically decoupled and implying that changes in physicochemical conditions within the first few hours of formation largely influence the outcome of the formed structure of tau and can be adjusted to modulate the phase behaviour of tau (Fig. 6c). These findings provide a motivation for further investigations of the potential relevance of observed differences in β-sheet rich aggregation and the formation of amorphous, solid-like tau assemblies, as well as the formation of tau intermediate states in disease through cellular experiments and animal models.

It is interesting to explore the mechanistic underpinnings of the observed differences between β-sheet rich aggregation and the formation of amorphous, solid-like tau assemblies in different parts of the phase space. The tie-line measurements of tau and PEG show that the dense phase composition of the condensates changes across the phase space. As a consequence, tau condensates with different dense phase compositions exhibit different ageing behaviour, such that condensates formed at high PEG concentrations lose their reversibility faster. The formation of ordered β-sheet structures is observed to be enhanced within the condensate at high protein and moderate PEG concentrations, while being slowed down at high PEG concentrations. It was shown that PEG increases the dominance of tau and induces LLPS through enhancing tau-tau interactions. This could explain how LLPS can accelerate the nucleation of β-sheet-rich structures by increasing the concentration of tau and consequentially increasing tau-tau interactions, which agrees with our observations of β-sheet formation at moderate crowder concentrations. However, at high PEG concentrations, this effect is counteracted by the decrease in the condensate dense phase mobility as confirmed by FRAP measurements (see Fig. S8). The slow β-sheet formation kinetics in high-PEG solution are therefore a consequence of a lowered diffusivity (74). This effect appears sufficient to slow down β-sheet nucleation to an extent where it becomes kinetically arrested and does not occur during the experimental time frame.

Together, our findings highlight the importance of understanding the phase behaviour across the entire phase space to be able to distinguish between the pathways and processes leading to functional assemblies of tau or its pathological irreversible β-sheet-rich aggregates, and to be able to potentially design rescue pathways for tau from pathological phases.

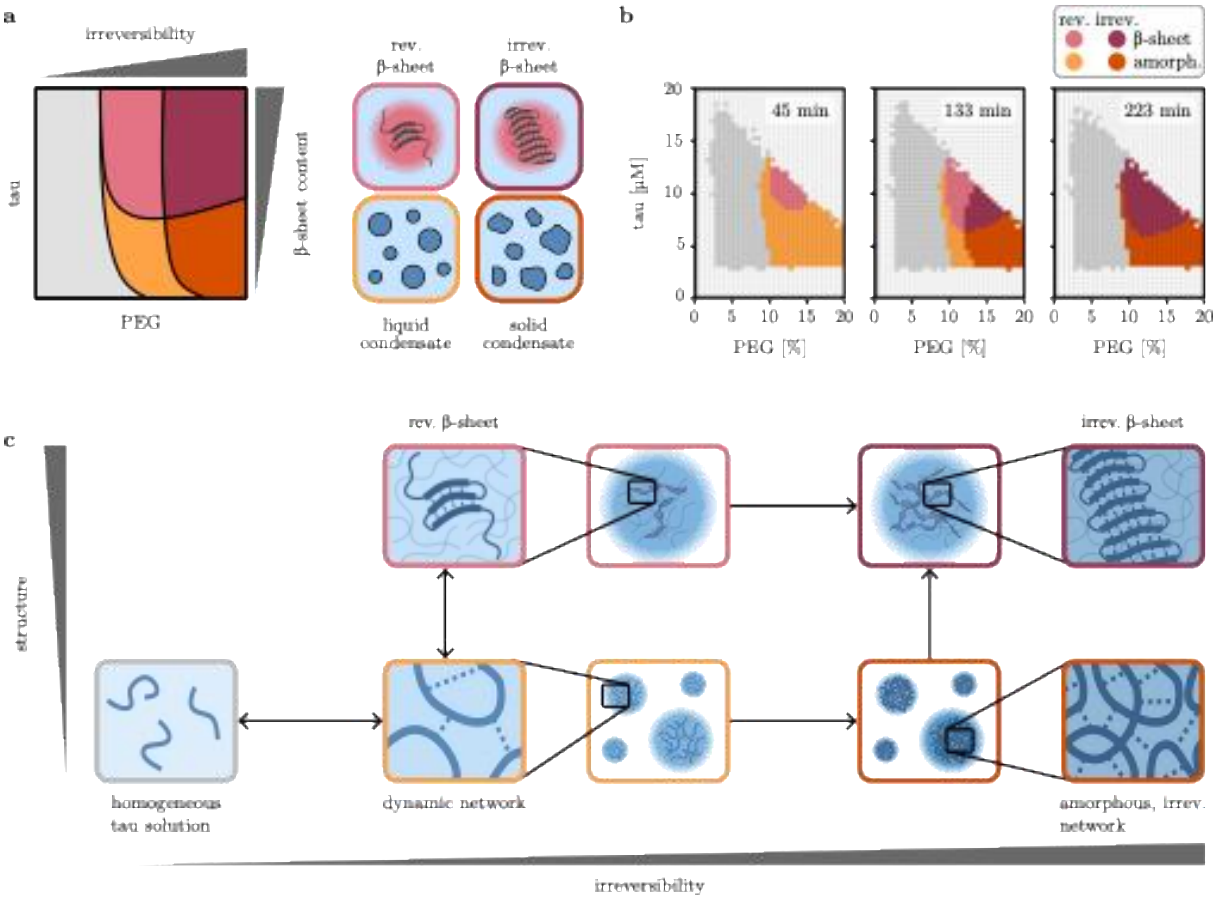

Figure 6. Integrating tau solubility and β-sheet formation in the tau-PEG phase space. **a.** Tau-PEG phase diagrams are overlaid to yield a phase diagram informing of the insolubility and β-sheet content of tau assemblies depending on the position in the phase space, distinguishing between liquid and solid condensates and the β-sheet propensity in the dense phase. **b.** Overlays of tau phase diagrams at 45, 133 and 223 min, respectively, for solubility and β-sheet formation indicating the reversibility and structure of tau assemblies as a function of time. **c.** Schematic indicating how physicochemical conditions and time determine the reversibility and structure of tau assemblies formed.

Conclusion

In this study, we uncover key mechanistic insights into the phase behaviour of tau, providing a more detailed understanding of the thermodynamic and kinetic determinants of tau's liquid-to-solid transition and β-sheet formation across the phase space. We reveal that tau can form liquid-like condensates, which age into insoluble amorphous gels or β-sheet rich aggregates through changes in physicochemical conditions such as protein concentration or crowding, and over time. Importantly, we find that the liquid-to-solid transition and the β-sheet formation of tau are decoupled processes following different kinetics as a function of the position in the phase space by using a microfluidic approach which integrates a dissolution assay with an amyloid-dye based detection across the phase space. Our findings imply that β-sheet rich structures formed at certain physicochemical conditions are reversible by dissolution within the first few hours of formation. Further, we demonstrate that heparin, a commonly used aggregation-enhancer, can modulate the phase behaviour of tau by interacting with tau and strengthening tau-tau interactions, leading to acceleration of tau condensate ageing. Mapping the kinetics of these phase transitions across the two-dimensional phase space allows us to identify specific regions where tau forms rescuable intermediate structures - a potential therapeutic target before β-sheet structures become irreversible.

To understand tau condensate ageing across the phase space, the molecular mechanisms underlying the liquid-to-solid transition and β-sheet formation were explored. Firstly, the measurements of tau dilute phase concentrations and dominance revealed that tau-tau interactions strengthen over time and with increasing crowding, suggesting that they are the main driving force of tau phase separation, while tau-PEG interactions add a small contribution. Furthermore, our tie-line measurements showed that the condensate dense phase undergoes compositional changes as a function of the phase space, rationalising how condensates formed at different conditions can exhibit different ageing behaviour, such that condensates formed at high PEG concentrations lose their reversibility faster. The formation of ordered β-sheet-rich structures from the condensate dense phase is accelerated through high tau concentrations inside the condensate and an increased number of tau-tau interactions, such that β-sheet formation from the dynamic liquid-like condensate dense phase occurs on the timescale of hours compared to their formation from solution (21). However, this effect is counteracted by the lowered mobility of tau in condensates formed under high-PEG conditions, which rate-limits the formation of β-sheets, such that the emergence of β-sheet rich structures is only observed in moderate-PEG conditions within the time frame of this experiment.

In more general terms, our findings show that the transition of tau from solution to an aggregated state is not a linear pathway from liquid-like to solid-like aged condensates to fibrillar aggregates. Our approach allows us to distinguish between the physicochemical conditions and kinetics leading to the formation of different tau states, revealing different pathways in condensate mediated aggregation. Furthermore, this diversity in the aggregation pathways that is uncovered by this study opens up new avenues to be able to potentially design intervention strategies to prevent tau from accessing parts of the phase space associated with pathology.

Materials and Methods

Protein phase diagrams were obtained using the microfluidic droplet screening platform "PhaseScan" (49). Droplet image analysis was performed using custom Python scripts (49). Detailed descriptions of the microfluidic methods, including droplet collection, incubation, dissolution ("Picoinjection"), and imaging, are provided in the SI Appendix. The SI Appendix further includes detailed descriptions of the materials used, and protocols for protein expression and purification, microfluidic device fabrication, confocal and epifluorescence microscopy of tau condensates and aggregates in bulk, fluorescence recovery after photobleaching (FRAP) experiments and Fourier transform infrared spectroscopic (FTIR) measurements. Supplementary figures are provided in the Appendix 01 and the datasets in the appendix Dataset S01.

References

1. S. Boyko, W. K. Surewicz, Tau liquid–liquid phase separation in neurodegenerative diseases. *Trends Cell Biol* 32, 611–623 (2022).
2. F. Chiti, C. M. Dobson, Protein Misfolding, Functional Amyloid, and Human Disease. *Annu Rev Biochem* 75, 333–366 (2006).
3. Y. Wang, E. Mandelkow, Tau in physiology and pathology. *Nat Rev Neurosci* 17, 22–35 (2016).
4. P. Chakraborty, M. Zweckstetter, Phase separation of the microtubule-associated protein tau. *Essays Biochem* 66, 1013–1021 (2022).
5. M. G. Spillantini, M. Goedert, Tau pathology and neurodegeneration. *Lancet Neurol* 12, 609–622 (2013).
6. V. M.-Y. Lee, M. Goedert, J. Q. Trojanowski, Neurodegenerative Tauopathies. *Annu Rev Neurosci* 24, 1121–1159 (2001).
7. Y. Zhang, K.-M. Wu, L. Yang, Q. Dong, J.-T. Yu, Tauopathies: new perspectives and challenges. *Mol Neurodegener* 17, 28 (2022).
8. P. Saha, N. Sen, Tauopathy: A common mechanism for neurodegeneration and brain aging. *Mech Ageing Dev* 178, 72–79 (2019).
9. M. E. Orr, A. C. Sullivan, B. Frost, A Brief Overview of Tauopathy: Causes, Consequences, and Therapeutic Strategies. *Trends Pharmacol Sci* 38, 637–648 (2017).
10. S. Banerjee, A. Ghosh, Structurally Distinct Polymorphs of Tau Aggregates Revealed by Nanoscale Infrared Spectroscopy. *J Phys Chem Lett* 12, 11035–11041 (2021).
11. Y. Losev, *et al.*, Novel model of secreted human tau protein reveals the impact of the abnormal N-glycosylation of tau on its aggregation propensity. *Sci Rep* 9, 2254 (2019).
12. J. Berriman, *et al.*, Tau filaments from human brain and from in vitro assembly of recombinant protein show cross-β structure. *Proceedings of the National Academy of Sciences* 100, 9034–9038 (2003).
13. C. Ballatore, V. M.-Y. Lee, J. Q. Trojanowski, Tau-mediated neurodegeneration in Alzheimer's disease and related disorders. *Nat Rev Neurosci* 8, 663–672 (2007).
14. G. Lee, C. J. Leugers, "chapter 8 - Tau and Tauopathies" in *Progress in Molecular Biology and Translational Science*, D. B. Teplow, Ed. (Academic Press, 2012), pp. 263–293.
15. K. Iqbal, F. Liu, C.-X. Gong, Tau and neurodegenerative disease: the story so far. *Nat Rev Neurol* 12, 15–27 (2016).
16. I. Saha, *et al.*, The AAA+ chaperone VCP disaggregates Tau fibrils and generates aggregate seeds in a cellular system. *Nat Commun* 14, 560 (2023).
17. F. Dou, *et al.*, Chaperones increase association of tau protein with microtubules. *Proceedings of the National Academy of Sciences* 100, 721–726 (2003).
18. B. Eftekharzadeh, *et al.*, Tau Protein Disrupts Nucleocytoplasmic Transport in Alzheimer's Disease. *Neuron* 99, 925-940.e7 (2018).
19. M. D. Weingarten, A. H. Lockwood, S. Y. Hwo, M. W. Kirschner, A protein factor essential for microtubule assembly. *Proceedings of the National Academy of Sciences* 72, 1858–1862 (1975).
20. L. I. Binder, A. Frankfurter, L. I. Rebhun, The distribution of tau in the mammalian central nervous system. *Journal of Cell Biology* 101, 1371–1378 (1985).
21. D. C. Rodriguez Camargo, *et al.*, Proliferation of Tau 304–380 Fragment Aggregates through Autocatalytic Secondary Nucleation. *ACS Chem Neurosci* 12, 4406–4415 (2021).

22. S. F. Banani, H. O. Lee, A. A. Hyman, M. K. Rosen, Biomolecular condensates: Organizers of cellular biochemistry. *Nat Rev Mol Cell Biol* [Preprint] (2017).
23. A. A. Hyman, C. A. Weber, F. Jülicher, Liquid-liquid phase separation in biology. *Annu Rev Cell Dev Biol* [Preprint] (2014).
24. H. R. Kilgore, R. A. Young, Learning the chemical grammar of biomolecular condensates. *Nat Chem Biol* (2022).
25. P. Li, *et al.*, Phase transitions in the assembly of multivalent signalling proteins. *Nature* 483, 336–340 (2012).
26. G. Tesei, T. K. Schulze, R. Crehuet, K. Lindorff-Larsen, Accurate model of liquid–liquid phase behavior of intrinsically disordered proteins from optimization of single-chain properties. *Proceedings of the National Academy of Sciences* 118, e2111696118 (2021).
27. A. Hernández-Vega, *et al.*, Local Nucleation of Microtubule Bundles through Tubulin Concentration into a Condensed Tau Phase. *Cell Rep* 20, 2304–2312 (2017).
28. S. Ambadipudi, J. Biernat, D. Riedel, E. Mandelkow, M. Zweckstetter, Liquid–liquid phase separation of the microtubule-binding repeats of the Alzheimer-related protein Tau. *Nat Commun* 8, 275 (2017).
29. S. Boyko, K. Surewicz, W. K. Surewicz, Regulatory mechanisms of tau protein fibrillation under the conditions of liquid–liquid phase separation. *Proceedings of the National Academy of Sciences* 117, 31882–31890 (2020).
30. S. Boyko, X. Qi, T.-H. Chen, K. Surewicz, W. K. Surewicz, Liquid–liquid phase separation of tau protein: The crucial role of electrostatic interactions. *Journal of Biological Chemistry* 294, 11054–11059 (2019).
31. S. Wegmann, *et al.*, Tau protein liquid–liquid phase separation can initiate tau aggregation. *EMBO J* 37, e98049 (2018).
32. R. Tan, *et al.*, Microtubules gate tau condensation to spatially regulate microtubule functions. *Nat Cell Biol* 21, 1078–1085 (2019).
33. A. Savastano, *et al.*, Disease-Associated Tau Phosphorylation Hinders Tubulin Assembly within Tau Condensates. *Angewandte Chemie International Edition* 60, 726–730 (2021).
34. P. Li, *et al.*, Liquid − liquid phase separation of tau: Driving forces, regulation, and biological implications. *Neurobiol Dis* 183, 106167 (2023).
35. S. K. Rai, A. Savastano, P. Singh, S. Mukhopadhyay, M. Zweckstetter, Liquid–liquid phase separation of tau: From molecular biophysics to physiology and disease. *Protein Science* 30, 1294–1314 (2021).
36. N. M. Kanaan, C. Hamel, T. Grabinski, B. Combs, Liquid-liquid phase separation induces pathogenic tau conformations in vitro. *Nat Commun* 11, 2809 (2020).
37. S. Jonchhe, W. Pan, P. Pokhrel, H. Mao, Small Molecules Modulate Liquid-to-Solid Transitions in Phase-Separated Tau Condensates. *Angewandte Chemie International Edition* (2022). https://doi.org/10.1002/anie.202113156.
38. J. Wen, *et al.*, Conformational Expansion of Tau in Condensates Promotes Irreversible Aggregation. *J Am Chem Soc* 143, 13056–13064 (2021).
39. T. Ukmar-Godec, S. Wegmann, M. Zweckstetter, Biomolecular condensation of the microtubule-associated protein tau. *Semin Cell Dev Biol* 99, 202–214 (2020).
40. A. Patel, *et al.*, A Liquid-to-Solid Phase Transition of the ALS Protein FUS Accelerated by Disease Mutation. *Cell* 162, 1066–1077 (2015).
41. S. Li, *et al.*, Mechanism underlying liquid-to-solid phase transition in fused in sarcoma liquid droplets. *Physical Chemistry Chemical Physics* 24, 19346–19353 (2022).

42. S. Mukherjee, *et al.*, Liquid-liquid Phase Separation of α-Synuclein: A New Mechanistic Insight for α-Synuclein Aggregation Associated with Parkinson's Disease Pathogenesis. *J Mol Biol* 435, 167713 (2023).
43. A. S. Sawner, *et al.*, Modulating α-Synuclein Liquid–Liquid Phase Separation. *Biochemistry* 60, 3676–3696 (2021).
44. S. Ray, *et al.*, α-Synuclein aggregation nucleates through liquid–liquid phase separation. *Nat Chem* 12, 705–716 (2020).
45. S. T. Dada, *et al.*, Spontaneous nucleation and fast aggregate-dependent proliferation of α-synuclein aggregates within liquid condensates at neutral pH. *Proceedings of the National Academy of Sciences* 120, e2208792120 (2023).
46. S. T. Dada, *et al.*, Pharmacological inhibition of α-synuclein aggregation within liquid condensates. *Nat Commun* 15, 3835 (2024).
47. J. Jackson, *et al.*, Actin-nucleation promoting factor N-WASP influences alpha-synuclein condensates and pathology. *Cell Death Dis* 15, 304 (2024).
48. L. Brodin, D. Milovanovic, S. O. Rizzoli, O. Shupliakov, α-Synuclein in the Synaptic Vesicle Liquid Phase: Active Player or Passive Bystander? *Front Mol Biosci* Volume 9-2022 (2022).
49. W. E. Arter, *et al.*, Biomolecular condensate phase diagrams with a combinatorial microdroplet platform. *Nat Commun* 13, 7845 (2022).
50. A. R. Abate, T. Hung, P. Mary, J. J. Agresti, D. A. Weitz, High-throughput injection with microfluidics using picoinjectors. *Proceedings of the National Academy of Sciences* 107, 19163–19166 (2010).
51. M. Brzezinski, *et al.*, Protein-Specific Crowding Accelerates Aging in Protein Condensates. *Biomacromolecules* 26, 2060–2075 (2025).
52. D. Qian, *et al.*, Dominance analysis to assess solute contributions to multicomponent phase equilibria. *Proceedings of the National Academy of Sciences* 121, e2407453121 (2024).
53. D. Qian, *et al.*, Molecular mechanisms of condensate modulation from energy-dominance analysis. *Phys Rev Appl* 23, 64017 (2025).
54. D. Qian, *et al.*, Tie-Line Analysis Reveals Interactions Driving Heteromolecular Condensate Formation. *Phys Rev X* 12, 41038 (2022).
55. D. Qian, *et al.*, Linking modulation of bio-molecular phase behaviour with collective interactions. *bioRxiv* 2023.11.02.565376 (2023). https://doi.org/10.1101/2023.11.02.565376.
56. H. Ausserwöger, *et al.*, Biomolecular condensates sustain pH gradients at equilibrium driven by charge neutralisation. *bioRxiv* 2024.05.23.595321 (2024). https://doi.org/10.1101/2024.05.23.595321.
57. C. M. Fischer, *et al.*, Temperature-induced changes in protein interactions control RNA recruitment to G3BP1 condensates. *bioRxiv* 2024.02.02.578543 (2024). https://doi.org/10.1101/2024.02.02.578543.
58. H. Ausserwöger, *et al.*, Quantifying collective interactions in biomolecular phase separation. *Nat Commun* 16, 7724 (2025).
59. S. Najafi, *et al.*, Liquid–liquid phase separation of Tau by self and complex coacervation. *Protein Science* 30, 1393–1407 (2021).
60. S. Boyko, X. Qi, T.-H. Chen, K. Surewicz, W. K. Surewicz, Liquid-liquid phase separation of tau protein: The crucial role of electrostatic interactions. *Journal of Biological Chemistry* 294, 11054–11059 (2019).

61. H. Ausserwöger, *et al.*, Quantifying collective interactions in biomolecular phase separation. *bioRxiv* 2023.05.31.543137 (2023). https://doi.org/10.1101/2023.05.31.543137.
62. J. Nyman, G. M. Day, Static and lattice vibrational energy differences between polymorphs. *CrystEngComm* 17, 5154–5165 (2015).
63. J. G. Wood, S. S. Mirra, N. J. Pollock, L. I. Binder, Neurofibrillary tangles of Alzheimer disease share antigenic determinants with the axonal microtubule-associated protein tau (tau). *Proceedings of the National Academy of Sciences* 83, 4040–4043 (1986).
64. T. C. Gamblin, *et al.*, Caspase cleavage of tau: Linking amyloid and neurofibrillary tangles in Alzheimer's disease. *Proceedings of the National Academy of Sciences* 100, 10032–10037 (2003).
65. M. Biancalana, S. Koide, Molecular mechanism of Thioflavin-T binding to amyloid fibrils. *Biochimica et Biophysica Acta (BBA) - Proteins and Proteomics* 1804, 1405–1412 (2010).
66. E. Pretorius, M. J. Page, L. Engelbrecht, G. C. Ellis, D. B. Kell, Substantial fibrin amyloidogenesis in type 2 diabetes assessed using amyloid-selective fluorescent stains. *Cardiovasc Diabetol* 16, 141 (2017).
67. D. C. Rodriguez Camargo, *et al.*, Proliferation of Tau 304–380 Fragment Aggregates through Autocatalytic Secondary Nucleation. *ACS Chem Neurosci* 12, 4406–4415 (2021).
68. R. P. Sear, Nucleation: theory and applications to protein solutions and colloidal suspensions. *Journal of Physics: Condensed Matter* 19, 033101 (2007).
69. W. Zhang, *et al.*, Heparin-induced tau filaments are polymorphic and differ from those in Alzheimer's and Pick's diseases. *Elife* 8, e43584 (2019).
70. H. K. Paudel, W. Li, Heparin-induced Conformational Change in Microtubule-associated Protein Tau as Detected by Chemical Cross-linking and Phosphopeptide Mapping *. *Journal of Biological Chemistry* 274, 8029–8038 (1999).
71. N. Sibille, *et al.*, Structural Impact of Heparin Binding to Full-Length Tau As Studied by NMR Spectroscopy. *Biochemistry* 45, 12560–12572 (2006).
72. M. Goedert, *et al.*, Assembly of microtubule-associated protein tau into Alzheimer-like filaments induced by sulphated glycosaminoglycans. *Nature* 383, 550–553 (1996).
73. I. Stroganova, Z. Toprakcioglu, H. Willenberg, T. P. J. Knowles, A. M. Rijs, Unraveling the Structure and Dynamics of Ac-PHF6-NH2 Tau Segment Oligomers. *ACS Chem Neurosci* 15, 3391–3400 (2024).
74. H. Wang, F. M. Kelley, D. Milovanovic, B. S. Schuster, Z. Shi, Surface tension and viscosity of protein condensates quantified by micropipette aspiration. *Biophysical Reports* 1, 100011 (2021).

Conflicts of interest

The authors declare no conflicts of interest.

Acknowledgements

We thank David Weitz for helpful discussions. The research leading to these results has received funding from the European Research Council under the European Union's Horizon 2020 research and innovation program through the ERC grant DiProPhys (agreement ID 101001615) (C.M.F., I.A.E., T.S., I.B., T.P.J.K.) and the Marie Skłodowska-Curie grant MicroREvolution (agreement no. 101023060) (T.S.), the Ron Thomson Research Fellowship in Alzheimer's Disease (Z.T.), Pembroke College Cambridge (Z.T.), the Swiss National Science Foundation (grant no. 222094, L.-T.D.), Innovationfund

Denmark (L.D., D.O.), the Francis and Augustus Newman Foundation (C.M.F., I.A.E., T.S., T.P.J.K.), the National Natural Science Foundation of China (31920103011 and 32371281) (S.P.), (22477132, 32171443 and 22477132) (S.W.), the Beijing Natural Science Foundation of China (5254039) (J.W), Transition Bio (R.S.), Wavebreak Therapeutics (I.A.E.), the National Laboratory of Biomacromolecules (S.P.) the Cambridge Centre for Misfolding Diseases (T.P.J.K.) and the Finlay family.

Author contribution

C.M.F., I.A.E, T.S., and T.P.J.K. designed and conceptualised the study. C.M.F., I.A.E., T.S., I.B., Z.T. and D.Q. performed investigations. S.W, S.P. and T.P.J.K. provided materials and methods. C.M.F., I.A.E., T.S., I.B. Z.T., D.Q., L.-T.D., R.S. and L.D. interpreted and analysed the data. C.M.F. wrote the original draft of the paper. All authors discussed the results, reviewed, edited and contributed to the final manuscript.

Correspondence

Correspondence and requests for materials should be addressed to Tuomas P. J. Knowles (tpjk2@cam.ac.uk).

Data availability

Data used in the study are included in the manuscript and/or supporting information.